PHOTONICS Research

Integrated optical switches based on Kerr symmetry breaking in microresonators

Yaojing Zhang,[1,2,†] Shuangyou Zhang,[1,3,†] Alekhya Ghosh,[1,4] Arghadeep Pal,[1,4] George N. Ghalanos,[1,5] Toby Bi,[1,4] Haochen Yan,[1,4] Hao Zhang,[1,6] Yongyong Zhuang,[7] Lewis Hill,[1] and Pascal Del'Haye[1,4,*]

[1]Max Planck Institute for the Science of Light, 91058 Erlangen, Germany
[2]School of Science and Engineering, The Chinese University of Hong Kong, Shenzhen, Shenzhen 518172, China
[3]Department of Electrical and Photonics Engineering, Technical University of Denmark, Kgs. Lyngby 2800, Denmark
[4]Department of Physics, Friedrich Alexander University Erlangen-Nuremberg, 91058 Erlangen, Germany
[5]Akhetonics GmbH, 10823 Berlin, Germany
[6]Key Laboratory of Radar Imaging and Microwave Photonics, Ministry of Education, Nanjing University of Aeronautics and Astronautics, Nanjing 210016, China
[7]Electronic Materials Research Laboratory, Key Laboratory of the Ministry of Education & International Center for Dielectric Research, School of Electronic Science and Engineering, Faculty of Electronic and Information Engineering, Xi'an Jiaotong University, Xi'an 710049, China
[†]These authors contributed equally to this work.
*Corresponding author: pascal.delhaye@mpl.mpg.de

Received 16 September 2024; revised 29 October 2024; accepted 4 November 2024; posted 5 November 2024 (Doc. ID 542111); published 17 January 2025

With the rapid development of the Internet of Things and big data, integrated optical switches are gaining prominence for applications in on-chip optical computing, optical memories, and optical communications. Here, we propose a novel approach for on-chip optical switches by utilizing the nonlinear optical Kerr effect induced spontaneous symmetry breaking (SSB), which leads to two distinct states of counterpropagating light in ring resonators. This technique is based on our first experimental observation of on-chip symmetry breaking in a high-Q (9.4×10^6) silicon nitride resonator with a measured SSB threshold power of approximately 3.9 mW. We further explore the influence of varying pump powers and frequency detunings on the performance of SSB-induced optical switches. Our work provides insights into the development of new types of photonic data processing devices and provides an innovative approach for the future implementation of on-chip optical memories.

https://doi.org/10.1364/PRJ.542111

1. INTRODUCTION

With the fast development and rapid adoption of all-optical data processing, integrated optical switches are expected to have an important impact on enhancing the speed, reducing power consumption, and minimizing the size of telecommunication systems and optical computing devices [1–3]. Integrated optical switches usually rely on mechanisms such as the thermo-optic effect or carrier dispersion effect to alter the refractive index of materials, allowing for switching between two discrete states. The Mach–Zehnder interferometer (MZI) [4], the microring resonator (MRR) [5], and the hybrid MRR and MZI [6] are the commonly employed structures. Over the last decades, considerable efforts have been made to improve the performance of integrated optical switches in terms of speed, power efficiency, bandwidth, compactness, and so on. Recently, phase change materials (PCMs) integrated with silicon devices have shown great potential as optical switches for further improving the speed performance. These materials can rapidly switch between two stable states and maintain them [7–9].

In the field of optical physics, it is known that spontaneous symmetry breaking (SSB) caused by the nonlinear Kerr effect can exhibit two different states from slight changes as optical switches, which have been revealed across numerous nonlinear optical systems, including nanolasers [10], nanophotonic Bose–Hubbard dimer [11], metamaterials [12], and microresonators [13–17]. In a single optical microresonator, SSB can be observed from the Kerr-interaction between two counterpropagating light waves [13,14,18,19] or polarization states [20–22]. In the context of bi-directionally pumped microresonators, SSB is caused by instability of the intracavity power. Beyond the threshold pump power, a small deviation between the counterpropagating light powers results in a large resonance frequency difference of the initially equal resonator modes in clockwise (CW) and counterclockwise (CCW) directions.

This leads to a strong optical nonreciprocity in a symmetry broken resonator. The chirality with unbalanced CW and CCW modes has various applications that have been proposed for optical switches [23], gyroscopes [24], isolators [25–27], and single-particle detection [28–30]. However, until now, SSB-induced switches have not been reported on chips.

Here, we propose to utilize the SSB in a Si_3N_4 resonator for novel on-chip optical switches. With bi-directional pumping involving two counterpropagating light waves, we observe the emergence of the SSB at a threshold power of 3.9 mW. Every time we cross the nonlinear threshold power, we observe a switching selection of either the CW or CCW state being dominant. The Si_3N_4 resonator has an intrinsic quality (Q) factor of 9.4×10^6. Finally, a hysteresis loop in the two directions is experimentally investigated at different pump powers and frequency detunings, indicated for optical switches.

2. RESULTS AND ANALYSIS

A. Principle of Symmetry Breaking

Symmetry breaking in a bi-directionally pumped Kerr resonator originates from the difference of Kerr resonance shift induced by the self-phase modulation for copropagating photons and the cross-phase modulation affecting counterpropagating photons [31]. If two counterpropagating light waves have identical frequencies but different intra-cavity powers inside a resonator, they will see different detunings with respect to the resonance frequency. Theoretically, for a resonator structure in Fig. 1(a), two light fields are injected with the same frequency and power from the left and right sides of the bus waveguide, i.e., P_L and P_R. The two light fields circulate in CW and CCW directions within the resonator and can interact with each other. As indicated in Fig. 1(b), when the powers of the two intra-cavity light fields are below the nonlinear threshold, the measured transmission spectra are identical in both directions with the resonance frequency of both directions being degenerated. However, if we increase the input powers, the different nonlinear refractive index changes for the two directions will lead to different resonance frequencies for the counterpropagating modes. Practically, the laser power and laser frequency unavoidably have small fluctuations, which can introduce slight differences in power and frequency between the two counterpropagation light waves. If a resonator has a high Q factor, the power difference will be strongly built up within the resonator through the Kerr symmetry breaking. Above the threshold power, the two counterpropagating resonator modes have different resonance frequencies. The resonator mode with higher power will see a smaller frequency shift and will be closer to the pump laser frequency, while the weaker resonator mode has a strong shift induced by cross-phase modulation and will be pushed away from the pump laser frequency [14]. This resonance frequency difference increases with increasing pump power. When the power fluctuations of the pump laser are random, the two light waves will randomly choose one of the two states, enabling the switching between the two light states which follows the hysteresis loop in the right panel of Fig. 1(b).

The optical field amplitudes propagating in the CW (E_+) and CCW (E_-) directions in a resonator can be written as [32,33]

$$\frac{\partial E_\pm}{\partial \tau} = \sqrt{\kappa_{ex}} E_{in,\pm} - \left[\frac{\kappa}{2} + i(\delta - g_k|E_\pm|^2 - 2g_k|E_\mp|^2)\right] E_\pm, \tag{1}$$

where $E_{in,+}$ and $E_{in,-}$ are the amplitudes of the input beams in CW and CCW directions, and δ is the frequency detuning between the input pump frequency and the resonance frequency. The total loss in the resonator is $\kappa = \kappa_{ex} + \kappa_0$, where κ_{ex} is the coupling loss and κ_0 is the internal loss. The Kerr nonlinear coefficient is $g_k = \frac{\hbar\omega_0^2 c n_2}{n_0^2 V_{eff}}$, where $\hbar$ is the Planck constant, ω_0 is the frequency of the pump mode, c is the speed of light, $V_{eff} = 2\pi R A_{eff}$ is the mode volume of a resonator with radius R and effective mode area A_{eff}, n_0 is the linear refractive index,

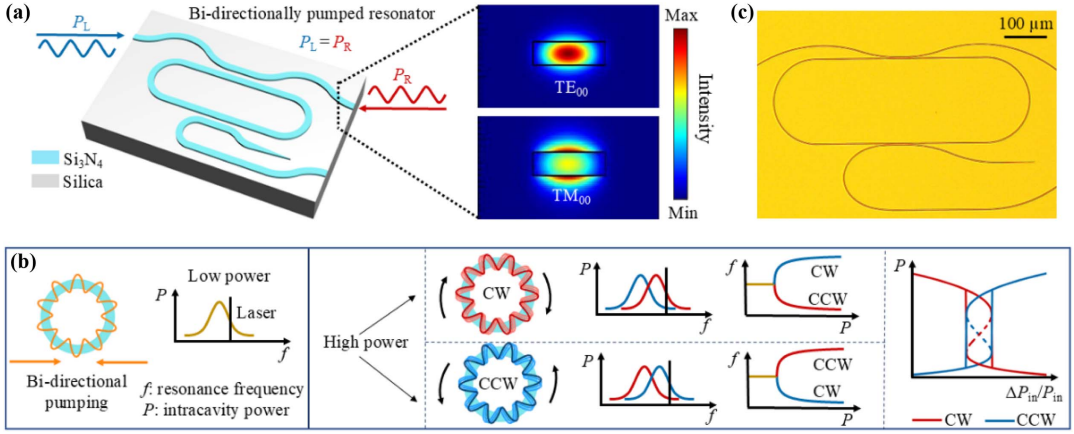

Fig. 1. Symmetry breaking of counterpropagating light in a high-Q Si_3N_4 resonator. (a) Schematic of the Kerr-nonlinearity-induced interaction of light in the Si_3N_4 resonator. Two counterpropagating light waves with the same frequency and power are injected from the left and right sides of the bus waveguide, which can support both TE_{00} and TM_{00} modes. (b) For bi-directional pumping, at low pump power, the two counterpropagating waves generate standing waves and the resonant transmission spectra of the two light waves are identical (left panel). At high power, the resonator enters a state with clockwise or counterclockwise circulating light. In this symmetry-breaking state, the optical modes in different directions have different resonance frequencies (middle panels). Increasing the optical power in the non-dominant direction enables switching between the counterpropagating light states. This switching behavior follows a hysteresis (right panel). (c) Microscope image of the Si_3N_4 resonator.

and n_2 is the nonlinear refractive index. The circulating powers in the CW and the CCW directions (P_{CW} and P_{CCW}) are proportional to the square of the fields, i.e., $P_{CW} \propto |E_+|^2$ and $P_{CCW} \propto |E_-|^2$. The threshold power of SSB is $P_{th} = \frac{1.54\pi n_0^2 V_{eff}}{\eta n_2 \lambda Q_L Q_i}$, where η is the coupling efficiency, λ is the pump wavelength, and the Q_L and Q_i factors are the loaded and intrinsic Q factors [14]. Aiming at low-threshold power SSB, the resonator is expected to have a small mode volume, high nonlinear refractive index, and high Q factor. Note that a higher Q factor especially helps to lower the threshold power because of the $1/Q^2$ dependence, which requires low-loss resonators.

The waveguide loss is determined by the material loss, scattering loss, and bending loss [34]. The scattering loss is related to the mode overlap with the sidewall roughness. A wide waveguide can reduce the mode overlap with the sidewall. Compared to the fundamental transverse electric (TE_{00}) mode, the fundamental transverse magnetic (TM_{00}) mode can have lower mode overlap, hence reducing the scattering loss and having a higher Q factor [34]. Here, we design the resonator with a waveguide width of 2 μm to support both TM_{00} and TE_{00} modes. To achieve a low bending loss, we select a bending radius of 100 μm for the resonator with 400-nm Si_3N_4 thickness, which can have a negligible bending loss according to our simulations. Details on the fabrication of Si_3N_4 resonators can be found in Refs. [35,36]. The fabricated Si_3N_4 resonator is shown in Fig. 1(c).

B. SSB-Induced Optical Switches in High-Q Si_3N_4 Resonators

The experimental setup for investigating SSB in the Si_3N_4 resonator is shown in Fig. 2(a). Continuous-wave light from a tunable laser serves as the pump light for both CW and CCW modes. The pump light is amplified by an erbium-doped fiber amplifier (EDFA) and subsequently divided into two pathways, directed to the left and right sides of the resonator's bus waveguide. Before coupling the pump light into the bus waveguide, two variable optical attenuators and polarization controllers (PCs) are used to control the pump powers and adjust the polarization state of the light. Two optical circulators are used to separately monitor the CW and CCW transmission spectra using two photodetectors (PDs). Both CW and CCW transmission spectra are recorded by an oscilloscope (OSC). In the measurement, we first align the light polarization into quasi-TM polarization. We choose one TM_{00} resonance at a wavelength of 1603 nm with a Q_i factor of 9.4×10^6 as shown in Fig. 2(b) for the SSB measurement [37]. By applying extended coupled-mode theory to fit the resonance transmission at the pump mode [38,39], we find that the coupling rate between the CW and CCW modes is around 16 MHz, which is comparable to the intrinsic linewidth. This leads to an asymmetric resonance lineshape as shown in Fig. 2(b), deviating from the typical Lorentzian profile. Despite the comparable coupling rates between CW and CCW modes, the SSB remains happening. The calculated SSB threshold is 3.8 mW. We experimentally investigate the SSB with input powers of 3.9 mW, 6.2 mW, and 15.7 mW, respectively, as shown in Figs. 2(c)–2(e). Each figure is obtained by sweeping the laser frequency with identical pump powers and exhibits randomly one of the two counterpropagating light states. With increasing pump power, the transmission spectrum exhibits a larger shift of resonance toward a lower frequency. More detailed dynamics of the symmetry breaking in high-Q Si_3N_4 resonators can be found in Appendix A, including theoretically calculated SSB spectra under different pump powers.

Next, we investigate the SSB behavior of TE_{00} resonance. We fabricate another resonator with a slightly wider waveguide width (3.45 μm) to reduce the TE_{00} mode overlap with the

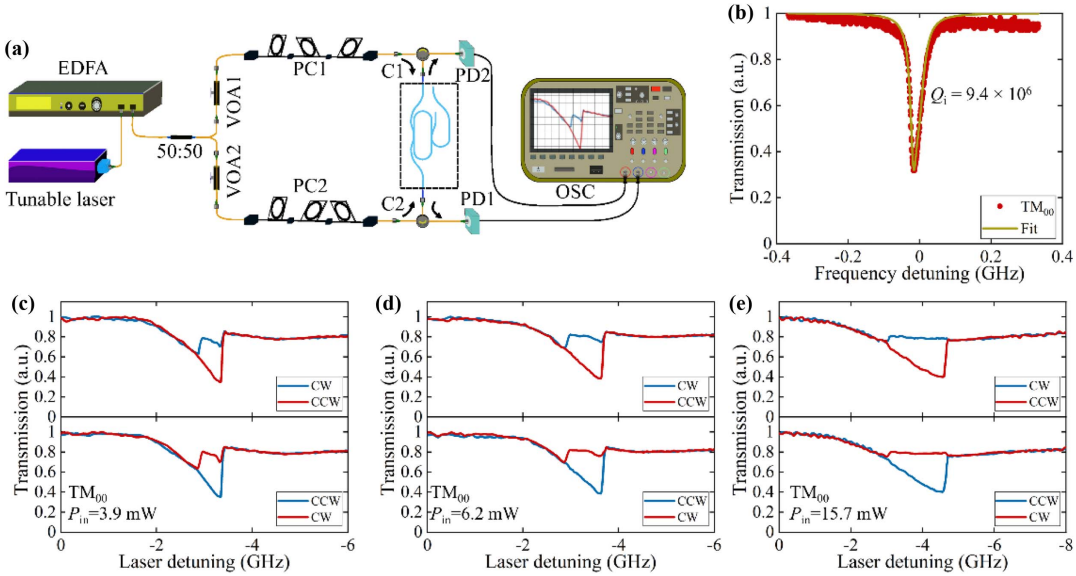

Fig. 2. Measurements of symmetry breaking at different powers for the TM_{00} resonance. (a) Experimental setup. The continuous-wave light from a tunable laser is amplified by an EDFA first and then split into two branches and coupled into the two sides of the bus waveguide. EDFA, erbium-doped fiber amplifier; VOA, variable optical attenuator; PC, polarization controller; C1, C2, circulators; PD1, PD2, photodetectors; OSC, oscilloscope. (b) Transmission spectrum of the TM_{00} mode at a wavelength of 1603 nm. Measured transmission spectra in CW and CCW directions at input pump powers of (c) 3.9 mW, (d) 6.2 mW, and (e) 15.7 mW, respectively.

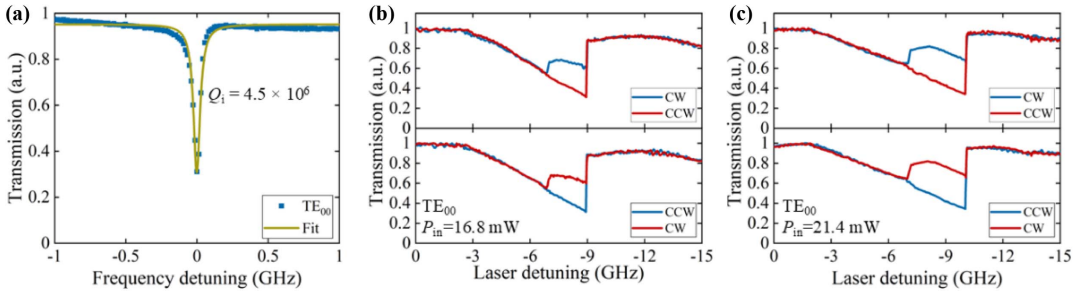

Fig. 3. Measurement of symmetry breaking for the TE_{00} resonance. (a) Transmission spectrum of the TE_{00} mode at a wavelength of 1572.6 nm. Measured transmission spectrum in CW and CCW directions at input pump powers of (b) 16.8 mW and (c) 21.4 mW, respectively.

sidewall roughness to further increase the Q factor of the TE_{00} mode. Figure 3(a) shows a transmission spectrum of a TE_{00} mode at a wavelength of 1572.6 nm with a Q_i factor of 4.5×10^6. This leads to the SSB threshold power of 14.8 mW. Experimentally, we start to observe the spontaneous symmetry broken CW and CCW states when the pump power increases to ~15 mW. Two examples of the SSB spectra at pump powers of 16.8 mW and 21.4 mW are shown in Figs. 3(b) and 3(c). Compared to the TM_{00} mode based SSB spectra in Fig. 2, the SSB spectrum of the TE_{00} mode is much broader. We attribute this to the lower Q factor and increased heating of the resonator due to optical losses. The full width at half maximum (FWHM) of the TE_{00} mode is about two times larger than that of the TM_{00} mode. Theoretically, unequal power distribution between the CW and CCW modes will result in one dominant state, which is suitable for optical isolation [25,26]. However, during the measurement, the presence of noise in the laser causes small fluctuations in the optical power. Thus, SSB can still occur with slight input power differences between CW and CCW modes.

An important feature of the Kerr-nonlinearity-induced symmetry breaking is the hysteresis property when changing the power ratio between P_{CW} and P_{CCW}, used as optical switches. Experimentally, employing the same experimental setup as in Fig. 2(a), we fixed the power of the CCW input and varied the power in the other direction up and down in steps of 0.05 dB. The hysteresis loop of the output powers is observed in the two directions at different power ratios of the input power, as shown in Fig. 4(a). In addition, we numerically investigate the SSB-based optical switching by increasing the average input power and frequency detuning as shown in Figs. 4(b)–4(e). Higher average input power and larger frequency detuning yield a broader stability range before the switching takes place, as summarized in Fig. 4(f).

For the spectra in Fig. 4, more optical power couples into the direction that has access to higher input power initially (CCW direction). This causes more shifts in the resonance in the other direction due to cross-phase modulation. Therefore, less optical power couples into the other direction (CW direction). Gradually increasing the input power in the CW direction only causes a slight increase in the coupled power as the resonance is shifted away from the cold resonance position. This continues even after the point when the input powers in the two directions become equal. However, after

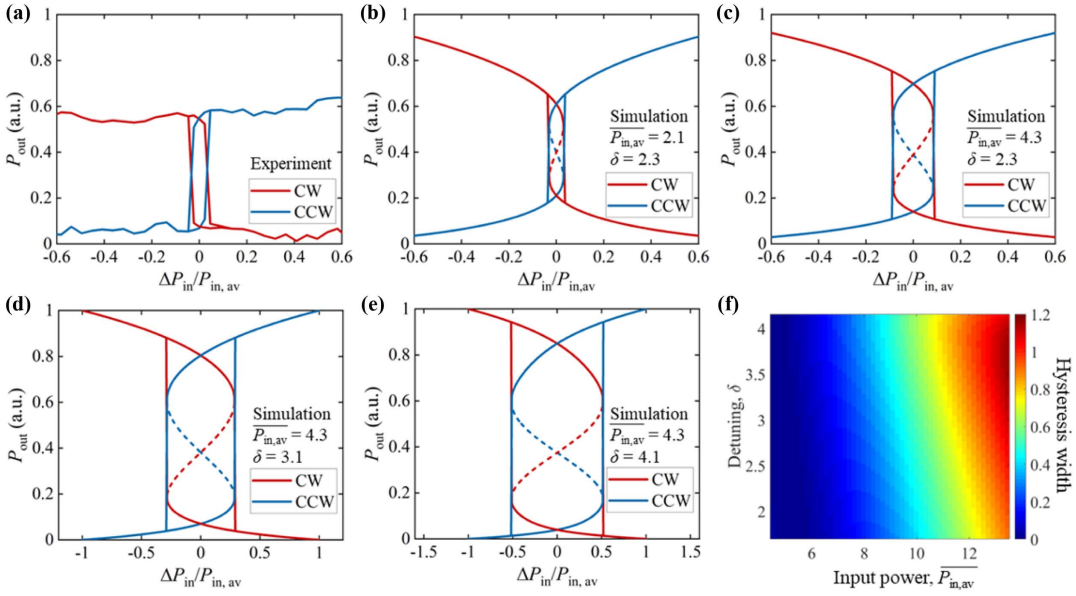

Fig. 4. Optical switching between CW and CCW light states. (a) Hysteresis measurement of the output powers in the two directions at different power ratios of the input power. (b), (c) Numerically simulated output power hysteresis with increasing input power. (d), (e) Simulated output power hysteresis with increased frequency detuning. (f) Hysteresis widths for different combinations of normalized average input power and detuning.

crossing the threshold power, the coupled optical power in the CW direction increases swiftly and eventually becomes equal to the coupled power in the opposite direction. Just a tiny increment of the input power in the CW direction after this point shifts the CCW resonance by a great amount, causing a sudden jump of the coupled powers and inversion of the dominant light state. When reversing the direction of the input power scan, the jump will occur far beyond the point of equal input powers. This causes a hysteresis in the coupled powers in the two directions and can be used for optical memories [23].

3. CONCLUSION

In summary, we report a novel approach for on-chip optical switches based on the first, to the best of our knowledge, experimental demonstration of on-chip spontaneous symmetry breaking of both TE and TM polarizations in high-Q single Si_3N_4 resonators. The Q-factors of the TM_{00} modes and TE_{00} modes are 9.4×10^6 and 4.5×10^6. Taking advantage of the high Q factor of the TM_{00} mode, the threshold power is measured as low as 3.9 mW. By further increasing the pump power to 6.2 mW, and 15.7 mW, we observe significant broadening of the laser detuning range that supports symmetry breaking. A hysteresis loop is also observed in high-Q Si_3N_4 resonators, used for optical switches. The influence of different pump powers and frequency detunings on the optical switches is investigated. Spontaneous symmetry breaking of the TE_{00} mode is observed at slightly higher pump powers of 15 mW. Based on the demonstrated symmetry breaking effect, the add–drop resonators in Fig. 2 can also be used for optical isolators [25–27]. In future research, the memory could be heterogeneously integrated with a semiconductor laser for optical computing [26]. Our demonstrated on-chip spontaneous symmetry breaking can also be applied to optical gyroscopes [24], random number generation [40,41], and optical neural networks [42,43].

APPENDIX A: SYMMETRY BREAKING DYNAMICS IN HIGH-Q Si_3N_4 RESONATORS

The normalized Lugiato–Lefever equation takes the form [32,33]

$$\frac{d\overline{E_\pm}}{dt}=\overline{E_{in,\pm}}-[\overline{E_\pm}+i(\overline{\delta}\,\overline{E_\pm}-|\overline{E_\pm}|^2\overline{E_\pm}-2|\overline{E_\mp}|^2\overline{E_\pm})] \tag{A1}$$

with the following substitutions:

$$\overline{\delta}=\frac{2\delta}{\kappa},\quad \overline{E_\pm}=\sqrt{\frac{2g_k}{\kappa}}E_\pm,\quad t=\frac{\kappa}{2}\tau,\quad \overline{E_{in,\pm}}=\sqrt{\frac{8\kappa_{ex}g_k}{\kappa^3}}E_{in,\pm}.$$

In steady state, Eq. (A1) takes the form

$$\overline{E_{in,\pm}}-[\overline{E_\pm}+i(\overline{\delta}\,\overline{E_\pm}-|\overline{E_\pm}|^2\overline{E_\pm}-2|\overline{E_\mp}|^2\overline{E_\pm})]=0. \tag{A2}$$

From Eq. (A2), we can get

$$|\overline{E_-}|^2=\frac{-(|\overline{E_+}|^4-\overline{\delta}|\overline{E_+}|^2)\pm\sqrt{|\overline{E_{in,+}}|^2|\overline{E_+}|^2-|\overline{E_+}|^4}}{2|\overline{E_+}|^2}, \tag{A3a}$$

$$[1+(\overline{\delta}-|\overline{E_-}|^2-2|\overline{E_+}|^2)^2]|\overline{E_-}|^2=|\overline{E_{in,-}}|^2. \tag{A3b}$$

Using the condition $|\overline{E_{in,-}}|^2=|\overline{E_{in,+}}|^2$ or $P_{in,+}=P_{in,-}=P_{in}$ in Eq. (A3), we can obtain the analytical solutions of transmitted powers in the CW and CCW directions. The analytical solutions are depicted by the dashed lines in Fig. 5. The numerical scan of Eq. (A1) for increasing detuning yields the result that will be observed typically in an experiment. During the scanning process, each detuned value in Eq. (A1) is evolved for a long enough time to bring the system to a steady state. To replicate the detuning scans as in experiments, the initial values of the fields for each detuning value are set to the steady state of the previous detuning value.

For each case in Fig. 5, at lower detuning (magnitude) the two fields remain symmetric. After a certain threshold, a pitchfork bifurcation occurs between the circulating intensities and thus the transmitted powers in the two directions, originating in the spontaneous symmetry breaking (SSB) region. The analytical solution shows a horn-like shape of the SSB bubble; i.e., the bubble folds on itself creating an optical bistability. In the SSB region, the simulated circulating field intensities follow the horn shape (one along the top branch and one along the bottom branch); however, at the sharp corner they jump to the symmetric topmost solution line. The large gap between the horn edge and the lower branch of the optical bistability within the SSB bubble hinders the system from accessing the lower branch of the bubble and continues up to the closing of the SSB bubble. For calculating the hysteresis associated with SSB, we rewrite Eqs. (A3a) and (A3b) in terms of

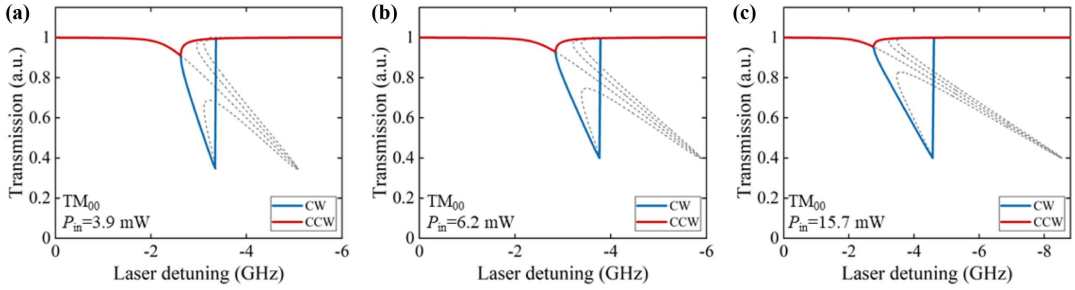

Fig. 5. Calculated spectra of symmetry breaking under different powers for TM_{00}-mode resonance. Simulated transmission spectra from CW and CCW directions under input pump powers of (a) 3.9 mW, (b) 6.2 mW, and (c) 15.7 mW, respectively, shown by the solid lines. Corresponding analytical solutions are depicted by the dashed lines.

the following variables: $2\overline{P_{\mathrm{in,av}}} = |\overline{E_{\mathrm{in,-}}}|^2 + |\overline{E_{\mathrm{in,+}}}|^2$, $\delta P = |\overline{E_{\mathrm{in,-}}}|^2 - |\overline{E_{\mathrm{in,+}}}|^2$, where the normalized average input power ($\overline{P_{\mathrm{in,av}}}$) is related to the unnormalized average input power ($P_{\mathrm{in,av}}$) by the formula $\overline{P_{\mathrm{in,av}}} = \frac{8\kappa_{\mathrm{ex}} g_0}{\hbar\omega\kappa^3} P_{\mathrm{in,av}}$.

Funding. Max-Planck-Gesellschaft; H2020 European Research Council (756966); The Chinese University of Hong Kong, Shenzhen (UDF01003527).

Acknowledgment. We thank Dr. Olga Lohse for the help with EBL exposure, Dr. Florentina Gannott for the help with the etching process, and Dr. Irina Harder and Mr. Alexander Gumann for useful discussions about device fabrication.

Disclosures. The authors declare no conflicts of interest.

Data Availability. Data underlying the results presented in this paper are not publicly available at this time but may be obtained from the authors upon reasonable request.

REFERENCES

1. X. Chen, J. Lin, and K. Wang, "A review of silicon-based integrated optical switches," Laser Photon. Rev. **17**, 2200571 (2023).
2. X. Tu, C. Song, T. Huang, *et al.*, "State of the art and perspectives on silicon photonic switches," Micromachines **10**, 51 (2019).
3. Z. Chai, X. Hu, F. Wang, *et al.*, "Ultrafast all-optical switching," Adv. Opt. Mater. **5**, 1600665 (2017).
4. T. Kita and M. Mendez-Astudillo, "Ultrafast silicon MZI optical switch with periodic electrodes and integrated heat sink," J. Lightwave Technol. **39**, 5054–5060 (2021).
5. Y. Huang, Q. Cheng, Y.-H. Hung, *et al.*, "Multi-stage 8 × 8 silicon photonic switch based on dual-microring switching elements," J. Lightwave Technol. **38**, 194–201 (2019).
6. Z. Guo, L. Lu, L. Zhou, *et al.*, "16 × 16 silicon optical switch based on dual-ring-assisted Mach–Zehnder interferometers," J. Lightwave Technol. **36**, 225–232 (2017).
7. Y. Li, F. Liu, G. Han, *et al.*, "Design of an electric-driven nonvolatile low-energy-consumption phase change optical switch," Nanotechnology **32**, 405201 (2021).
8. C. Zhang, M. Zhang, Y. Xie, *et al.*, "Wavelength-selective 2×2 optical switch based on a $Ge_2Sb_2Te_5$-assisted microring," Photon. Res. **8**, 1171–1176 (2020).
9. K. J. Miller, R. F. Haglund, Jr., and S. M. Weiss, "Optical phase change materials in integrated silicon photonic devices," Opt. Mater. Express **8**, 2415–2429 (2018).
10. P. Hamel, S. Haddadi, F. Raineri, *et al.*, "Spontaneous mirror-symmetry breaking in coupled photonic-crystal nanolasers," Nat. Photonics **9**, 311–315 (2015).
11. B. Garbin, A. Giraldo, K. J. Peters, *et al.*, "Spontaneous symmetry breaking in a coherently driven nanophotonic Bose-Hubbard dimer," Phys. Rev. Lett. **128**, 053901 (2022).
12. M. Liu, D. A. Powell, I. V. Shadrivov, *et al.*, "Spontaneous chiral symmetry breaking in metamaterials," Nat. Commun. **5**, 4441 (2014).
13. Q.-T. Cao, H. Wang, C.-H. Dong, *et al.*, "Experimental demonstration of spontaneous chirality in a nonlinear microresonator," Phys. Rev. Lett. **118**, 033901 (2017).
14. L. Del Bino, J. M. Silver, S. L. Stebbings, *et al.*, "Symmetry breaking of counter-propagating light in a nonlinear resonator," Sci. Rep. **7**, 43142 (2017).
15. E. Verhagen and A. Alù, "Optomechanical nonreciprocity," Nat. Phys. **13**, 922–924 (2017).
16. A. Ghosh, A. Pal, L. Hill, *et al.*, "Controlled light distribution with coupled microresonator chains via Kerr symmetry breaking," Photon. Res. **12**, 2376–2389 (2024).
17. A. Ghosh, A. Pal, S. Zhang, *et al.*, "Phase symmetry breaking of counterpropagating light in microresonators for switches and logic gates," arXiv, arXiv:2407.16625 (2024).
18. M. T. M. Woodley, L. Hill, L. Del Bino, *et al.*, "Self-switching Kerr oscillations of counterpropagating light in microresonators," Phys. Rev. Lett. **126**, 043901 (2021).
19. Y. Rah and K. Yu, "Demonstration of spontaneous symmetry breaking in self-modulated ring resonators," Phys. Rev. Res. **6**, 013234 (2024).
20. N. Moroney, L. Del Bino, S. Zhang, *et al.*, "A Kerr polarization controller," Nat. Commun. **13**, 398 (2022).
21. F. Copie, M. T. M. Woodley, L. Del Bino, *et al.*, "Interplay of polarization and time-reversal symmetry breaking in synchronously pumped ring resonators," Phys. Rev. Lett. **122**, 013905 (2019).
22. B. Garbin, J. Fatome, G.-L. Oppo, *et al.*, "Asymmetric balance in symmetry breaking," Phys. Rev. Res. **2**, 023244 (2020).
23. L. Del Bino, N. Moroney, and P. Del'Haye, "Optical memories and switching dynamics of counterpropagating light states in microresonators," Opt. Express **29**, 2193–2203 (2021).
24. J. M. Silver, L. Del Bino, M. T. M. Woodley, *et al.*, "Nonlinear enhanced microresonator gyroscope," Optica **8**, 1219–1226 (2021).
25. L. Del Bino, J. M. Silver, M. T. M. Woodley, *et al.*, "Microresonator isolators and circulators based on the intrinsic nonreciprocity of the Kerr effect," Optica **5**, 279–282 (2018).
26. A. D. White, G. H. Ahn, K. V. Gasse, *et al.*, "Integrated passive nonlinear optical isolators," Nat. Photonics **17**, 143–149 (2023).
27. A. D. White, G. H. Ahn, R. Luhtaru, *et al.*, "Unified laser stabilization and isolation on a silicon chip," Nat. Photonics **18**, 1305–1311 (2024).
28. B. Peng, Ş. K. Özdemir, M. Liertzer, *et al.*, "Chiral modes and directional lasing at exceptional points," Proc. Natl. Acad. Sci. USA **113**, 6845–6850 (2016).
29. I. Shomroni, S. Rosenblum, Y. Lovsky, *et al.*, "All-optical routing of single photons by a one-atom switch controlled by a single photon," Science **345**, 903–906 (2014).
30. X. Zhang, Q.-T. Cao, Z. Wang, *et al.*, "Symmetry-breaking-induced nonlinear optics at a microcavity surface," Nat. Photonics **13**, 21–24 (2019).
31. L. Hill, G.-L. Oppo, M. T. M. Woodley, *et al.*, "Effects of self-and cross-phase modulation on the spontaneous symmetry breaking of light in ring resonators," Phys. Rev. A **101**, 013823 (2020).
32. A. Tikan, J. Riemensberger, K. Komagata, *et al.*, "Emergent nonlinear phenomena in a driven dissipative photonic dimer," Nat. Phys. **17**, 604–610 (2021).
33. M. T. M. Woodley, J. M. Silver, L. Hill, *et al.*, "Universal symmetry-breaking dynamics for the Kerr interaction of counterpropagating light in dielectric ring resonators," Phys. Rev. A **98**, 053863 (2018).
34. T. A. Huffman, G. M. Brodnik, C. Pinho, *et al.*, "Integrated resonators in an ultralow loss Si_3N_4/SiO_2 platform for multifunction applications," IEEE J. Sel. Top. Quantum Electron. **24**, 5900209 (2018).
35. S. Zhang, T. Bi, I. Harder, *et al.*, "Low-temperature sputtered ultralow-loss silicon nitride for hybrid photonic integration," Laser Photon. Rev. **18**, 2300642 (2024).
36. Y. Zhang, S. Zhang, T. Bi, *et al.*, "Geometry optimization for dark soliton combs in thin multimode silicon nitride microresonators," Opt. Express **31**, 41420–41427 (2023).
37. S. Zhang, T. Bi, and P. Del'Haye, "On-the-fly precision spectroscopy with a dual-modulated tunable diode laser and Hz-level referencing to a cavity," Adv. Photon. **6**, 046003 (2024).
38. Q. Li, A. A. Eftekhar, Z. Xia, *et al.*, "Unified approach to mode splitting and scattering loss in high-*Q* whispering-gallery-mode microresonators," Phys. Rev. A **88**, 033816 (2013).
39. M. H. Pfeiffer, J. Liu, A. S. Raja, *et al.*, "Ultra-smooth silicon nitride waveguides based on the Damascene reflow process: fabrication and loss origins," Optica **5**, 884–892 (2018).

40. B. Shen, H. Shu, W. Xie, *et al.*, "Harnessing microcomb-based parallel chaos for random number generation and optical decision making," Nat. Commun. **14**, 4590 (2023).
41. L. Quinn, G. Xu, Y. Xu, *et al.*, "Random number generation using spontaneous symmetry breaking in a Kerr resonator," Opt. Lett. **48**, 3741–3744 (2023).
42. H. Deng and M. Khajavikhan, "Parity–time symmetric optical neural networks," Optica **8**, 1328–1333 (2021).
43. Y. Bai, X. Xu, M. Tan, *et al.*, "Photonic multiplexing techniques for neuromorphic computing," Nanophotonics **12**, 795–817 (2023).